Biosensors and Bioelectronics 74 (2015) 71–77

Contents lists available at ScienceDirect

Biosensors and Bioelectronics

journal homepage: www.elsevier.com/locate/bios

Highly exposed Pt nanoparticles supported on porous graphene for electrochemical detection of hydrogen peroxide in living cells

Jian Liu [a], Xiangjie Bo [a,*], Zheng Zhao [b], Liping Guo [a,*]

[a] Faculty of Chemistry, Northeast Normal University, Changchun 130024, PR China
[b] School of Chemical Engineering and Technology, Harbin Institute of Technology, Harbin 150001, PR China

ARTICLE INFO

Article history:
Received 14 April 2015
Received in revised form
16 June 2015
Accepted 18 June 2015
Available online 20 June 2015

Keywords:
Porous graphene
Pt nanoparticles
Cell tracking
Electrochemical biosensor
Nonenzymatic hydrogen peroxide detection

ABSTRACT

In this study, we developed a novel biosensor based on highly exposed Pt nanoparticles (Pt NPs) decorated porous graphene (PG) for the reliable detection of extracellular hydrogen peroxide (H_2O_2) released from living cells. The commercially available low-cost hydrophilic $CaCO_3$ spheres were used as template for preparing PG. The porous structure provided larger surface area and more active sites. Due to the porous structure of PG, the Pt NPs supported on PG were not secluded by aggregated graphene layers and were highly exposed to target molecules. Ultrafine Pt NPs were well dispersed and loaded on PG by a method of microwave assistance. Electrochemical performances of the Pt/PG nanocomposites modified glassy carbon electrode (GCE) were investigated. The electrocatalytic reduction of H_2O_2 showed a wide linear range from 1 to 1477 μM, with a high sensitivity of 341.14 μA mM^{-1} cm^{-2} and a limit of detection (LOD) as low as 0.50 μM. Moreover, the Pt/PG/GCE exhibited excellent anti-interference property, reproducibility and long-term storage stability. Because of these remarkable analytical advantages, the constructed sensor was used to determine H_2O_2 released from living cells with satisfactory results. The superior catalytic activity makes Pt/PG nanocomposites a promising candidate for electrochemical sensors and biosensors design.

1. Introduction

H_2O_2 is a common representative of reactive oxygen species (ROS) (Maruyama et al., 1995; Ohshima et al., 2003). It plays an important role in normal cellular growth and proliferation (Harman, 1981; Rhee 2006; Veal et al., 2007). Nevertheless, over production and accumulation of ROS in cells could lead to a series of cell damage and cause aging and disease, including cardiovascular disease, Alzheimer's disease and cancer (Pagliari et al., 2012; Trachootham et al., 2009; Wu et al., 2011). Hence, H_2O_2 is closely related to people's safety and health. The effectiveness of the fast and accurate detection of H_2O_2 is of critical importance. There are numerous kinds of methods developed for the detection of H_2O_2, for instance, titrimetry (Klassen et al., 1994), photometry (Lobnik and Ajlakovi, 2001), chemiluminescence (Zhang and Wong, 1999), high performance liquid chromatography (Effkemann et al., 1998) and electrochemistry (Liu et al., 2014; Zhang, 2008; Zhang et al., 2014b). Among these methods, the electrochemical technique has received considerable interest because of its easy operation, fast response, low detection limit and high sensitivity. In recent years, enzyme-based electrochemical sensors have witnessed an increasing interest because of their high efficiency, good selectivity and sensitivity (Privett et al., 2010). However, the enzyme-based sensors are limited by poor stability, environmental instability and a complicated immobilization procedure (Liu et al., 2010; Shoji and Freund, 2001). Therefore, non-enzymatic electrochemical sensors have received considerable attention in the past decades.

It has been found that noble metals possess outstanding electrocatalytic activity toward H_2O_2 redox reaction (Jou et al., 2014; Noh et al., 2012). Therein, Pt NPs have been demonstrated to lower the H_2O_2 oxidation/reduction overvoltage efficiently (Bo et al., 2011; Chu et al., 2007). The electrocatalytic activity of Pt catalyst is related with many factors, for instance, the size and distribution of Pt NPs and the support materials. Because of the high price of noble metal, it is desirable to minimize the amount used but to maximize the available surface area of the noble metal. Experiments prove that Pt NPs could disperse well on the surface of carbon materials, which leads to large surface area (Guo et al., 2010; Li et al., 2014). Some kinds of carbon nanomaterials have been used as support of Pt NPs, such as carbon nanotubes, ordered mesoporous carbon and graphene (Bo et al., 2010; Bragaru et al., 2014; Fang et al., 2012). Nonetheless, due to the low concentration of H_2O_2 in cell, the detection limit still needs to be improved. Thus,

* Corresponding authors. Fax: +86 0431 85099762.
E-mail addresses: baoxj133@nenu.edu.cn (X. Bo), guolp078@nenu.edu.cn (L. Guo).

http://dx.doi.org/10.1016/j.bios.2015.06.042
0956-5663/

it is necessary to develop more effective nanomaterial as support.

Graphene (GR) is considered as a promising candidate for a variety of applications in the fields of chemistry, materials science and physics on account of its excellent mechanical, optical, electric properties and biocompatibility (Geim and Novoselov, 2007; Novoselov et al., 2004). In catalytic area, GR is often used as a supporting substrate, and it can enhance the catalytic activity (Akhavan et al., 2012). However, according to the unique 2D structure, GR sheets have a very tendency to aggregate during synthesis process, resulting in low specific surface area and restricting its electrochemical performance in electrochemistry (Wang et al., 2008). Meanwhile, active sites for electrochemical catalysis are easily sandwiched between GR sheets or deeply hidden inside the aggregated GR and not available for electrochemical catalysis. As a nanoparticle support, the nanoparticles are tending to secluded by the aggregated layers. Therefore, the alleviation of the aggregation of GR sheets can facilitate the exposure of nanoparticles and effectively increase the catalytic activity of GR-based catalysts. Construction of GR into porous structure can effectively prevent aggregation of GR sheets (Han et al., 2014; Jiang and Fan, 2014). Moreover, nanopores are advantageous for ions passing through (Sint et al., 2008). These advantages made PG an excellent supporting material. However, few works are available on the application of Pt NPs/porous GR as electrochemical sensors.

In this article, we fabricated a novel biosensor based on ultrafine Pt NPs decorated PG to determine H_2O_2 from living cells. Although nanoparticles/GR composites have been reported for the detection of H_2O_2 in living cells (Bai and Jiang, 2013; Sun et al., 2015; Zhang et al., 2014a), our methodology is special because: (1) the porous structure and large surface area favor the deposition of nanoparticles; (2) due to the porous structure and large surface, highly exposed nanoparticles supported on PG supply more surface active sites for catalysis of H_2O_2; (3) the confinement of H_2O_2 in the pores of PG results in a higher occurrence of H_2O_2-active site encounters and then a higher activity.

2. Materials and methods

2.1. Reagents and apparatus

H_2O_2 was purchased from Beijing Dingguo Biotechnology Co. Ltd. Nafion (5 wt%) was obtained from Sigma-Aldrich, while $H_2PtCl_6 \cdot 6H_2O$ and uric acid (UA), dopamine (DA), ascorbic acid (AA), acetamidophenol (AP) were obtained from Sinopharm Chemical Reagent Co., Ltd. The phosphate buffer solution (PBS pH 7.0), which was prepared using a combination of NaH_2PO_4, Na_2HPO_4 and H_3PO_4, was employed as a supporting electrolyte. All other reagents were at least of analytical grade and used as received. All aqueous solutions were prepared with double distilled water.

X-ray diffraction (XRD) patterns were obtained on an X-ray D/max-2200vpc (Rigaku Corporation, Japan) instrument operated at 40 kV and 20 mA using Cu Kα radiation (λ=0.15406 nm). The morphological characterizations were obtained with scanning electron microscopy (SEM, XL-30 ESEM, Philips Company) and transmission electron microscopy (TEM, JEM-2100F, Japan) operating at 200 kV. X-ray photoelectron spectroscopy (XPS) was measured using an ESCALAB 250 spectrometer (Thermo Electron Corp.) with Al Kα radiation (1486.6 eV) as the excitation source. Nitrogen adsorption–desorption isotherms were performed on ASAP 2020 (Micromeritics, USA). The Brunauer–Emmett–Teller (BET) method was used to calculate the specific surface area. The pore size distribution plot was obtained from the desorption branch of the isotherm by utilizing the Barrett–Joyner–Halenda (BJH) model. Thermogravimetric analysis (TGA) was performed on a TGA Q5000 (TA Instruments, USA).

Electrochemical experiments were performed with a CHI660C Electrochemical Analyzer (CH Instruments, China) in a conventional three-electrode cell. A modified GCE (3 mm diameter) serving as a working electrode. An Ag/AgCl (in saturated KCl solution) electrode served as a reference electrode, while a platinum wire used as the counter electrode. The electrolyte was purged with highly-purity nitrogen for 20 min to get the deoxygenated atmosphere. Phosphate-buffered saline containing 144 mg L^{-1} KH_2PO_4, 9000 mg L^{-1} NaCl, and 795 mg L^{-1} $Na_2HPO_4 \cdot 7H_2O$ was purchased from Invitrogen (10010), which was used for washing cells and balanced salt solution in the cell culture. All experiments were performed at room temperature.

2.2. Synthesis of PG

Graphene oxide (GO) was synthesized from natural graphite powder according to a modified Hummers and Offeman method (Hummers and Offeman, 1958). GO (0.6 g) was dispersed in 500 mL of distilled water. After ultrasonication for 6 h, hydrophilic $CaCO_3$ (0.6 g) were added into the slurry at the rate of 1:1 in mass, followed by stirring at room temperature for 3 h. Then the mixture was dried at 70 °C for 12 h. Next, the sample was grinded to powders, and tablet compressed. Afterward, calcination of the GO/$CaCO_3$ sample was conducted at 900 °C for 3 h under an N_2 flow at a heating rate of 3 °C min^{-1}. The CaO particles were washed away by using 15 wt% HCl solution. After washing with distilled water and ethanol repeatedly, PG sample denoted as PG-1 was obtained. The sample PG-1.5, which mass rate of $CaCO_3$ and GO was 1:1.5 was synthesized similarly by adding 0.9 g of $CaCO_3$ into GO slurry. The sample without $CaCO_3$ was synthesized in the similar way for comparison named as RGO.

2.3. Synthesis of Pt/PG composites

First, 20 mg of PG-1 was dispersed in 40 mL ethylene glycol followed by approximately 60 min of ultrasonication. Then an aqueous solution of 66 μL of H_2PtCl_6 (0.1 g mL^{-1}) was added to the above solution under stirring to obtain the Pt/PG nanocomposites named Pt_{21}/PG-1. The content of Pt NPs was determined by TGA (Fig. S3). After 10 min of ultrasonication, the solution was placed in the microwave oven for 2 min (power: 800 W). The suspension was isolated by centrifugation, followed by washing with ethyl alcohol and double distilled water several times. The obtained Pt_{21}/PG-1 was dried in the oven at 60 °C for 36 h. The Pt_{21}/PG-1.5, Pt_{21}/RGO, Pt_{11}/PG-1 and Pt_{41}/PG-1 samples were synthesized in addition in the similar way. Illustration of the preparation of Pt/PG is presented in Scheme 1.

2.4. Preparation of the modified electrodes

Prior to the modification, GCE was polished with 1, 0.3 and 0.05 μm alumina powder, respectively. Then rinsed with deionized water in an ultrasonic bath, and dried with high-purity nitrogen steam. Pt_{21}/PG-1 nanocomposites modified GCE was prepared by casting 5 μL of the Pt_{21}/PG-1 suspension (2 mg mL^{-1} in 0.1 wt% Nafion) on the GCE surface and dried in air. For comparison, Pt_{21}/PG-1.5/Nafion/GCE, Pt_{11}/PG-1/Nafion/GCE and Pt_{41}/PG-1/Nafion/GCE were also prepared with the same method.

2.5. Detection of H_2O_2 released from cells

HeLa cells (cervical cancer cell line) were cultured in a DMEM medium containing 10% fetal bovine serum, 100 units mL^{-1} penicillin, and 100 mg mL^{-1} streptomycin at 37 °C with 5% CO_2 in water vapor-saturated air atmosphere. HeLa cells grown in 25 cm^2 cell culture flasks were seeded in a 12-well plate (5×10^4 cells per

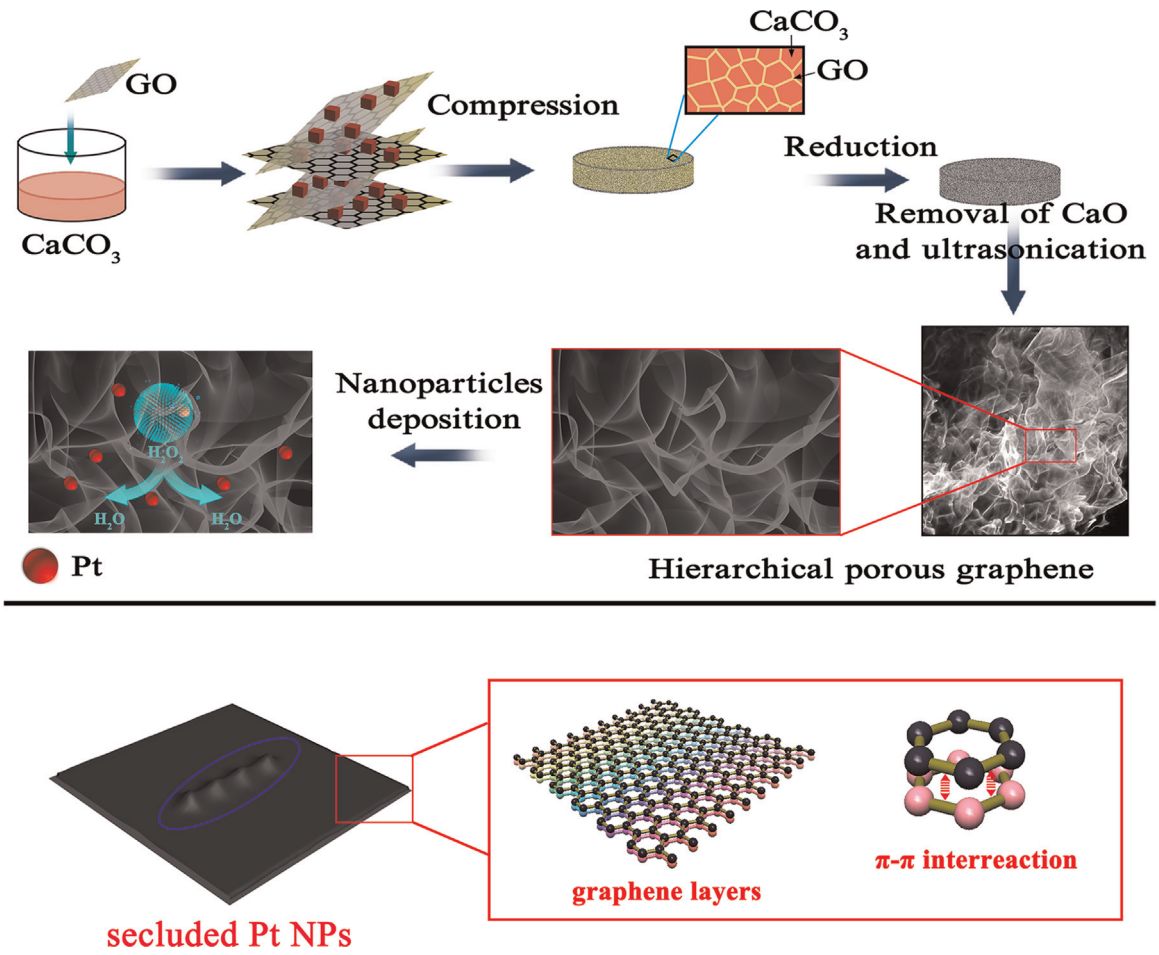

Scheme 1. Illustration of the preparation of Pt/PG samples.

well) for 24 h for electrochemical experiments. The media was removed and the cells were washed three times with phosphate-buffered saline, and then 3 mL phosphate-buffered saline was added for real sample measurements. The amperometric detection of the release flux of H_2O_2 from HeLa cells was performed using the Pt_{21}/PG-1/Nafion/GCE, which was placed inside the 12-well plate and exposed to the cell solution. CdTe QDs were injected into the buffer, and H_2O_2 produced from the cancer cell was monitored by amperometric measurements.

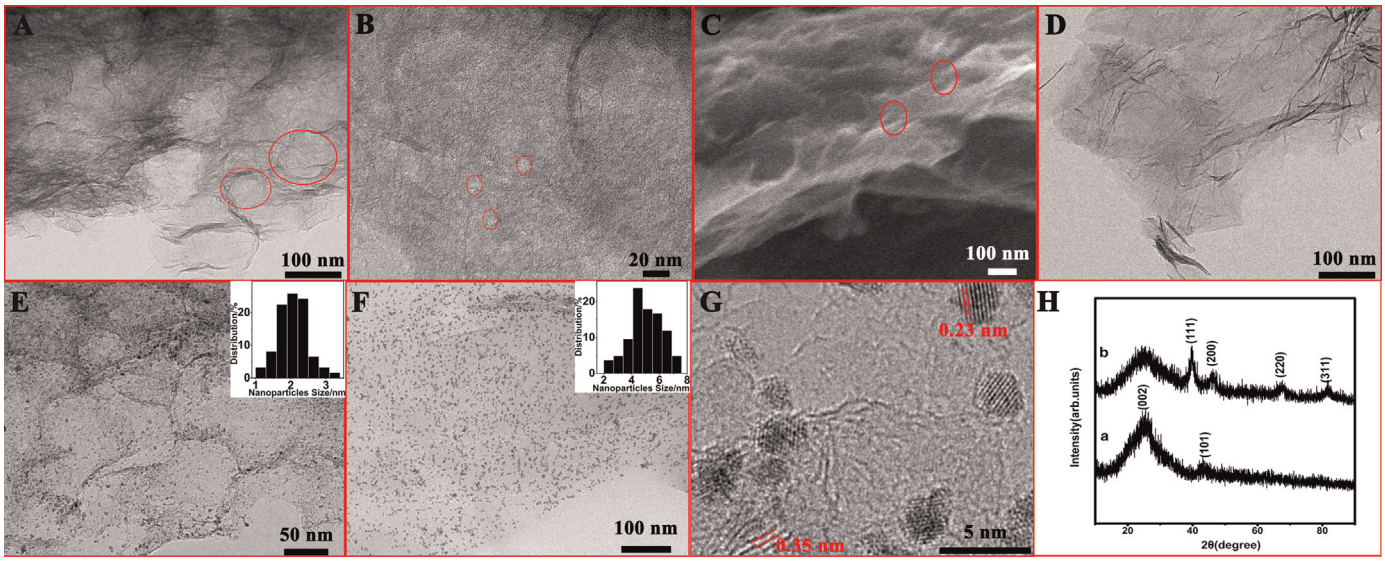

Fig. 1. (A) and (B) TEM images of PG with different magnifications. (C) SEM image of PG. (D) TEM image of RGO. (E) TEM image of Pt/PG. Inset indicates the particle size distribution of the Pt NPs on it. (F) TEM image of Pt/RGO. Inset shows the particle size distribution of the Pt NPs on it. (G) HRTEM image of Pt/PG. (H) Wide-angle XRD of (a) PG and (b) Pt/PG. (For interpretation of the references to color in this figure, the reader is referred to the web version of this article.)

3. Results and discussion

3.1. Characterization of PG and Pt/PG nanocomposites

The morphologies of PG and Pt/PG were characterized by TEM and SEM. Crumpled structure and well-developed porous structure can be observed from TEM images of PG (Fig. 1A and B). The micro-, meso- and macropores are tightly attached on PG sheets, which are marked by the red circles. During calcination, the $CaCO_3$ decomposes into CaO and CO_2, and CO_2 pushes and expands the GO layers to enlarge the pores. The macropores in Fig. 1A are generated by the removal of the CaO spheres and the size of macropores is consistent the size of $CaCO_3$ template (Fig. S1A). At the meantime, redox reaction between CO_2 and the carbon atom of GR causes the cleavage of C–C bonds of GR and produces the micro- and mesopores. Fig. 1C shows the SEM image of PG. It can be seen there are numerous nanosize pores (marked by the red circles). Thus, the PG could be defined as hierarchical porous GR. As contrast, RGO sample, which was prepared without $CaCO_3$ template, has no significant nanopores (Fig. 1D). Fig. 1E exhibits the TEM image of Pt NPs and many Pt NPs are well dispersed and located on the surface of PG. Inset of Fig. 1E illustrates the relevant histogram of the particle size distribution of Pt NPs. The sizes of Pt NPs on PG are between 1.01 and 3.42 nm. On counting 200 particles, the average diameter is 2.06 nm, as can be seen in the histogram. In contrast, Pt NPs supported on RGO are poorly dispersed and aggregate to large regiments (Fig. 1F). Their sizes are between 2.02 and 7.51 nm with a mean diameter of 5.25 nm (inset of Fig. 1F), which is much larger than that of Pt NPs on PG. The high surface area of PG can provide a good support for anchoring Pt NPs and prevent their aggregation. The high resolution TEM (HRTEM) image of Pt/PG (Fig. 1G) clearly reveals the detailed morphology of Pt/PG, in which all the Pt NPs are uniformly confined on the PG sheet. Moreover, it can be clearly seen that the lattice is 0.23 nm, corresponding to the (111) interplanar spacing of the face-centered cubic Pt NP. SEM images of RGO (Fig. S1B) shows RGO with no significant nanopores.

Fig. 1H displays XRD of PG and Pt/PG nanocomposites. A broad and a weak peak at 2θ of 25.9 and 43.0° are observed at PG sample (a), corresponding to the (002) and (101) diffractions of graphite, indicating the oxygen functional groups has been thermally removed under high temperature. After the reduction with H_2PtCl_6, the newly-appeared diffraction peaks located at 39.79°, 46.25°, 67.60° and 81.66°, corresponding to the (111), (200), (220) and (311) Pt facets respectively, demonstrate that Pt NPs exist in Pt/PG nanocomposites (Zhang et al., 2010; Zhou et al., 2010).

XPS study has been carried out to further determine the surface composition of GO and Pt/PG. It can be seen in Fig. 2A and B, C 1s peaks consist of four components including C–C (284.5 eV), C–O (286.3 eV), C=O (288.7 eV) and O=C–O (289.7 eV). After calcination the intensities of the carbon atoms become predominant, while the intensities of the carbon atoms bonded to oxygen are obviously reduced, indicating a fairly good thermal reduction. Fig. 2C shows XPS pattern of Pt 4f for Pt/PG. The Pt 4f 7/2 and 4f 5/2 lines appear at around 71.6 and 74.8 eV, respectively, which demonstrates the Pt/PG nanocomposites have been successfully synthesized. Fig. 2D exhibits XPS pattern of Ca 2p for Pt/PG, which is clearly that there is no Ca characteristic peak, indicating that CaO has been removed completely. Typical XPS spectra of PG and Pt/PG have been provided in Fig. S3, which also reflects the deposition of Pt NPs and effective removal of $CaCO_3$ template.

The attachment of the Pt NPs to PG was also proved by TGA (Fig. S4). The release of the mass occurs at around 350 °C, which is mainly because of the thermal decomposition of carbon materials in air atmosphere. The weight ratio of the Pt NPs to PG is estimated to be 0.21:0.79. So the sample is named as Pt_{21}/PG-1. The TGA of Pt_{11}/PG-1 and Pt_{41}/PG-1 are also presented.

The N_2 adsorption–desorption isotherms of PG sample (Fig. 2E) validates the presence of pores in PG by a type IV isotherm with a hysteresis loop in the middle and high relative pressure range. The BET specific surface area and pore volume of Pt/PG are 453.00 $m^2\,g^{-1}$ and 0.57 $cm^3\,g^{-1}$, which are higher than RGO sample (79.05 $m^2\,g^{-1}$ and 0.14 $cm^3\,g^{-1}$). The pore size distributions of PG and RGO are exhibited in the inset of Fig. 2E, which illustrate that PG have varying sizes of nanopores and a very narrow pore-size distribution centered at about 3 nm.

Fig. S5 depicts the CVs of Pt_{21}/RGO/Nafion/GCE and Pt_{21}/PG-1/Nafion/GCE in N_2-saturated 0.5 M H_2SO_4 solution at a scan rate of 50 mV s^{-1}. The electrochemical active surface area (EAS) of the Pt NPs supported on RGO and PG-1 can be estimated by measuring

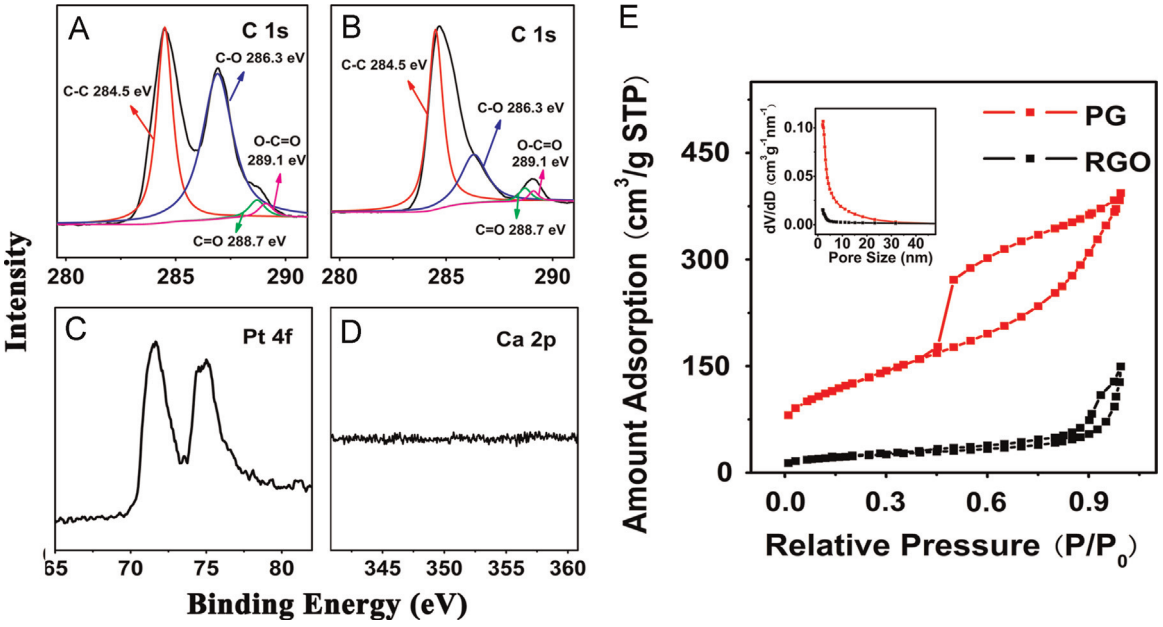

Fig. 2. XPS of C 1s of GO (A) and Pt/PG (B) nanocomposites. XPS of Pt 4f (C) and Ca 2p (D) of Pt/PG nanocomposites. (E) Nitrogen adsorption–desorption isotherms for RGO and PG-1 nanocomposites. Inset showed the pore size distribution of RGO and PG-1.

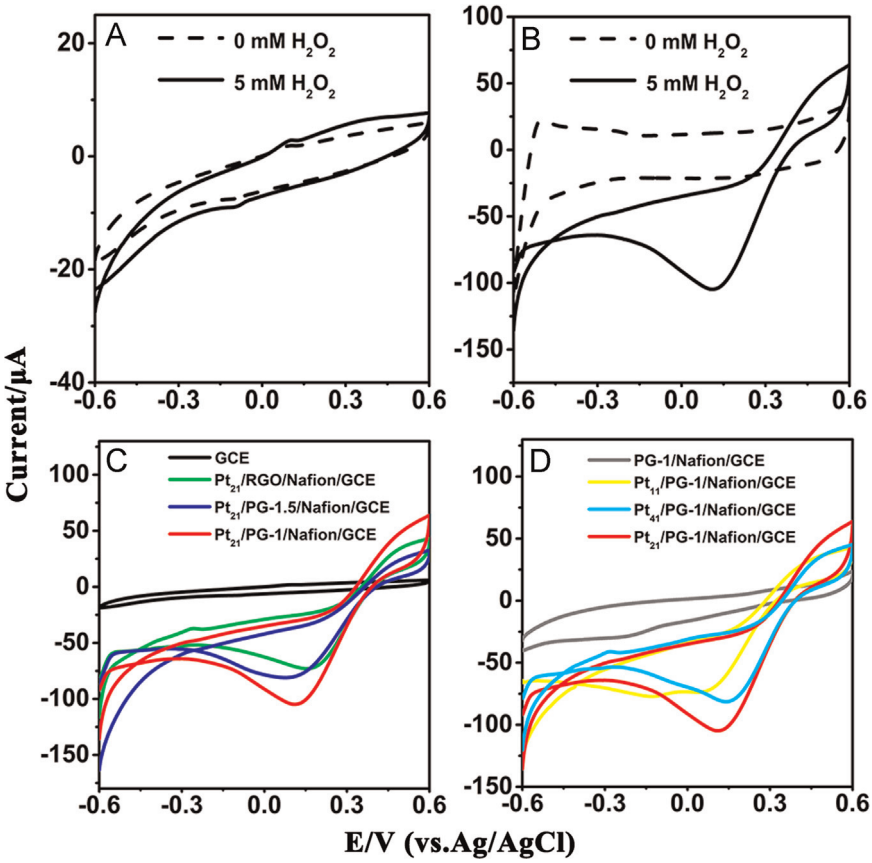

Fig. 3. CVs of (A) bare GCE, (B) Pt_{21}/PG-1/Nafion/GCE in 0.1 M PBS (pH 7.0) containing 0 and 5 mM H_2O_2. (C) CVs obtained in 0.1 M PBS (pH 7.0) containing 5 mM H_2O_2 at bare GCE, RGO/Nafion/GCE, Pt_{21}/PG-1.5/Nafion/GCE and Pt_{21}/PG-1/Nafion/GCE. Scan rate: 50 mV s^{-1} (D) CVs obtained in 0.1 M PBS (pH 7.0) containing 5 mM H_2O_2 at PG-1/Nafion/GCE, Pt_{11}/PG-1/Nafion/GCE, Pt_{41}/PG-1/Nafion/GCE, and Pt_{21}/PG-1/Nafion/GCE. Scan rate: 50 mV s^{-1}.

the charge using the hydrogen electroadsorption curves (Q_H) according to the following equation:

$$\text{EAS} = \frac{Q_H}{Q_{ref} \times \text{Pt loading}}$$

Q_H represents the charge of hydrogen adsorption/desorption and Q_{ref}=0.21 mC cm^{-2}, representing the surface density of the polycrystalline Pt electrode. The results show that the EAS of Pt_{21}/RGO and Pt_{21}/PG-1 are 38.78 m^2 g^{-1} and 52.84 m^2 g^{-1}, respectively. As can be seen, the porous structure leads to larger EAS, which attributes to high exposure of Pt NPs.

3.2. *Electrocatalytic reduction of H_2O_2 at Pt/PG/Nafion/GC electrode*

The electrochemical activity of the Pt/PG nanocomposites toward the H_2O_2 reduction was studied by cyclic voltammetry (CV). Fig. 3 displays the CVs of (A) bare GC and (B) Pt_{21}/PG-1/Nafion/GC electrodes in the absence and presence of 5.0 mM H_2O_2 in the N_2-saturated 0.1 M PBS solution (pH 7.0) at a scan rate of 50 mV s^{-1}. Upon addition of 5.0 mM H_2O_2, imperceptible current for the reduction of H_2O_2 is observed at (A) bare GCE, while the reduction peak current increases significantly for the (B) Pt_{21}/PG-1/Nafion/GCE. The maximum peak value of reduction current on Pt_{21}/PG-1/Nafion/GCE is −110.5 μA and the peak potential is 0.14 V, which are much higher and more positive than that on bare GCE. This result suggests that the Pt_{21}/PG-1/Nafion/GCE possesses efficient electrocatalytic activity toward the reduction of H_2O_2, which provides an approach for detecting H_2O_2.

The improvement of the electrochemical properties of the Pt/PG nanocomposites might be caused by the following reasons. First, the porous structure could avoid the agglomeration of GR sheets and enlarge the surface area. Meanwhile, interconnected pores may guarantee a fast diffusion. Such a structure is also easy to composite with Pt NPs. At last, the small size of Pt NPs in the composites may also contribute to the enhancement of the electrochemical performance.

During the thermal-reduction of GO, $CaCO_3$ decomposes at high temperature with the removal of CO_2. The CO_2 as pore formation agent could enhance the porosity of PG. At the meantime, redox reaction takes place between CO_2 and the carbon atom of GR, resulting in many micropores and defects, which could improve the porosity and surface area of PG and benefit to the deposition of Pt NPs. However, over redox reaction may reduce the yield of PG. Therefore, the ratio of GO and $CaCO_3$ is an important factor in this experiment. Fig. 3C shows CVs of bare GCE, Pt_{21}/RGO/Nafion/GCE, Pt_{21}/PG-1.5/Nafion/GCE and Pt_{21}/PG-1/Nafion/GCE in the presence of 5 mM H_2O_2. As can be seen in Fig. 3C, the Pt_{21}/PG-1/Nafion/GCE which mass ratio of $CaCO_3$ and GO is 1:1 has the lowest potential and the largest peak current density. This result suggests that Pt_{21}/PG-1/Nafion/GCE possesses the most efficient electrocatalytic activity toward the reduction of H_2O_2. The large discrepancy in activity between Pt_{21}/PG-1/Nafion/GCE and Pt_{21}/RGO/Nafion/GCE is due to the availability of surface active sites of Pt NPs. The porous structure of PG-1 facilitates the exposure of NPs, while the Pt NPs supported on RGO are secluded by aggregated GR layers. The highly exposed Pt NPs supported on PG-1 provides more active sites for reduction of H_2O_2.

The influence of the contents of Pt NPs has also been investigated. Fig. 3D displays CVs of PG-1/Nafion/GCE, Pt_{11}/PG-1/Nafion/GCE, Pt_{41}/PG-1/Nafion/GCE and Pt_{21}/PG-1/Nafion/GCE in the presence of 5 mM H_2O_2. As can be seen, Pt_{21}/PG-1/Nafion/GCE has the maximum peak value of reduction current. This may be

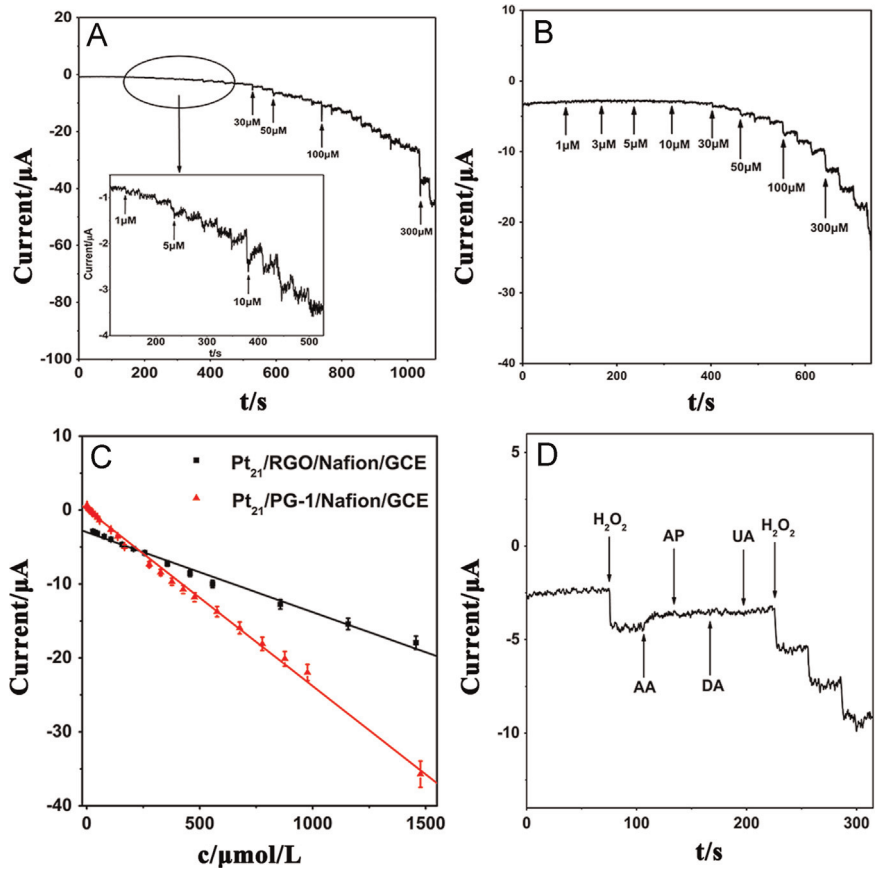

Fig. 4. Amperometric current–time curve of (A) Pt_{21}/PG-1/Nafion/GCE and (B) Pt_{21}/RGO/Nafion/GCE with successive additions of H_2O_2 at the potential of −0.1 V. Inset of (A) shows the amperometric response with successive addition of H_2O_2 at lower concentration. (C) The corresponding calibration plots between H_2O_2 concentration and current signal for Pt_{21}/PG-1/Nafion/GCE and Pt_{21}/RGO/Nafion/GCE. (D) Amperometric response of Pt_{21}/PG-1/Nafion/GCE at −0.1 V in PBS (pH 7.0) to successive addition of 0.1 mM H_2O_2, 0.1 mM AA, 0.1 mM AP, 0.1 mM DA, 0.1 mM UA and a second 0.1 mM H_2O_2.

attributed to the following reasons: Compared with Pt_{11}/PG-1 (Fig. S2A), Pt_{21}/PG-1 has higher loading amount of Pt NPs, which is favorable for accelerating the electron transfer. However, the agglomeration could be easily caused in the process of preparation and application if the amount of Pt NPs is too high, which is also proved by the TEM image of Pt_{41}/PG-1 (Fig. S2B). Due to the excellent electrochemical properties, Pt_{21}/PG-1/Nafion/GCE has been chosen for research in the following work.

3.3. *Amperometric performance of the Pt_{21}/PG-1/Nafion/GCE to H_2O_2 reduction*

The detection sensitivity for H_2O_2 on the relevant modified electrode has been further studied through amperometric study. Fig. 4A displays a typical amperometric response of Pt_{21}/PG-1/Nafion/GCE for H_2O_2 detection at pH 7.0 at −0.1 V. Inset of Fig. 4A exhibits the current–time response of low concentration of H_2O_2 at Pt_{21}/PG-1/Nafion/GCE. As shown in Fig. 4A, upon the successive additions of H_2O_2, the response of Pt_{21}/PG-1/Nafion/GCE is quickly and could reach the steady-state current within 3 s after the injection of H_2O_2, indicating a fast amperometric response to the reduction of H_2O_2. In contrast, the Pt_{21}/RGO/Nafion/GCE was also investigated, which reveals low amperometric response for the injection H_2O_2 (Fig. 4B). The comparison of corresponding calibration curves for Pt_{21}/PG-1/Nafion/GCE and Pt_{21}/RGO/Nafion/GCE are present in Fig. 4C. It also clearly shows that Pt_{21}/PG-1/Nafion/GCE displays a significantly enhanced sensitivity. For Pt_{21}/PG-1/Nafion/GCE, the linear regression equation is as follows: I (μA)= 0.0816 − 0.0239 C (μM) (R=0.998). The relevant linear range for the detection of H_2O_2 is from 1 to 1477 μM with a high sensitivity of 341.14 μA mM^{-1} cm^{-2}. The detection limit is calculated as 0.50 μM (ratio of signal-to-noise S/N=3). A comparison of linear range and detection limit for Pt_{21}/PG-1/Nafion/GCE with other H_2O_2 sensors reported in literature are summarized in Table S1. The data demonstrate the analytical parameters of Pt_{21}/PG-1/Nafion/GCE are comparable and even better than those obtained at several electrodes reported recently.

The influences of potential interferences of the Pt_{21}/PG-1/Nafion/GCE for the detection of H_2O_2 were also evaluated by the amperometric current–time method. Fig. 4D illustrates the amperometric response of the relevant sensor upon addition of 0.1 mM H_2O_2, 0.1 mM AA, 0.1 mM AP, 0.1 mM DA, 0.1 mM UA and a second 0.1 mM H_2O_2 in the same sample. There are remarkable current responses with the addition of 0.1 mM H_2O_2, while no obvious current responses are observed with the addition of 0.1 mM AA, AP, DA and UA. The CVs of AA, DA, UA, AP and H_2O_2 in the same solution have been presented in Fig. S6. With the addition of AA, DA, UA and AP, the current responses of H_2O_2 have no obvious change. The good selectivity is attributed to the low potential (−0.1 V) applied for detection.

The reproducibility and stability of Pt_{21}/PG-1/Nafion/GCE were further investigated. The relative standard deviation (RSD) of the current signal to H_2O_2 sensing is less than 6.8% for five measurements for the same electrode, indicating that the Pt_{21}/PG-1/Nafion/GCE has good reproducibility for the detection of H_2O_2. After successive 100 CV cycles of 5 mM H_2O_2, the current response retained to 85.3% of the original response (Fig. S7A). When the Pt_{21}/PG-1/Nafion/GCE was stored at room temperature for 14 days, the current response to 1 mM H_2O_2 retains 92.3% of its original value (Fig. S7B). The results further suggest the reliability of the Pt_{21}/PG-

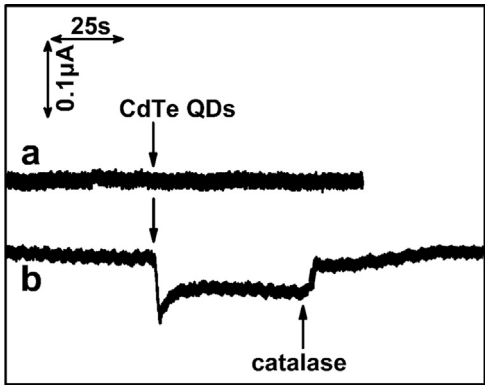

Fig. 5. Amperometric responses obtained at the Pt_{21}/PG-1/Nafion/GCE in the (a) absence and (b) presence of HeLa cells at −0.1 V with the addition of 0.4 mg mL^{-1} CdTe QDs and 400 units mL^{-1} catalase.

1/Nafion/GCE for determination of H_2O_2.

3.4. Detection of H_2O_2 release from living Cells

The H_2O_2 release in the human cervical cancer cell lines HeLa was monitored using the as-prepared Pt_{21}/PG-1/Nafion/GCE in phosphate-buffered saline (pH 7.4) under an applied potential of −0.1 V versus Ag/AgCl. Fig. 5 shows amperometric responses obtained at the Pt_{21}/PG-1/Nafion/GCE in the (a) absence and (b) presence of HeLa cells in N_2-saturated addition of CdTe QDs. With the addition of 0.4 mg mL^{-1} CdTe QDs, the cathodic current suddenly increased, while no response is attained in the solution without HeLa cells with the same addition of CdTe QDs. Recently, some researches indicate that CdTe QDs could induce cell death by generating ROS like H_2O_2 (Chen et al., 2012; Ipe et al., 2005). So it is used to stimulate the living cells to generate H_2O_2. In order to confirm whether the increased current is caused by the H_2O_2 produced from the cells after the addition of CdTe QDs, catalase solution was added to the solution, which is a selective scavenger of H_2O_2. After injection of catalase, the current response decreases to almost the background. Hereby, we can conclude that the increase of cathodic current response is caused by the release of H_2O_2. The current change is around 0.068 μA, corresponding to 0.57 μM H_2O_2, as calculated based on the regression equation from Fig. 4C. These results illustrate that Pt_{21}/PG-1/Nafion/GCE could be effectively used for reliable and durable determination of H_2O_2.

4. Conclusion

In conclusion, a nonenzymatic H_2O_2 sensor was fabricated based on hierarchical PG loading with Pt NPs. The porous structure is favorable for electrocatalysis. The Pt NPs are well-formed on PG with uniform size distribution. Electrochemical investigations indicate that the Pt/PG nanocomposites-modified electrode exhibits good catalysis and sensitivity for H_2O_2 detection. The as-prepared sensor provides a promising way to detect H_2O_2 released from the living cells because of the wide linear range, low LOD, excellent anti-interference property, good reproducibility and long-term storage stability.

Acknowledgments

Financial support from National Natural Science Foundation of China (201405011) is highly appreciated.

Appendix A. Supplementary material

Supplementary data associated with this article can be found in the online version at 10.1016/j.bios.2015.06.042.

References

Akhavan, O., Ghaderi, E., Aghayee, S., Fereydooni, Y., Talebi, A., 2012. J. Mater. Chem. 22 (27), 13773–13781.
Bai, J., Jiang, X., 2013. Anal. Chem. 85 (17), 8095–8101.
Bo, X., Bai, J., Qi, B., Guo, L., 2011. Biosens. Bioelectron. 28 (1), 77–83.
Bo, X., Bai, J., Wang, L., Guo, L., 2010. Talanta 81 (1-2), 339–345.
Bragaru, A., Vasile, E., Obreja, C., Kusko, M., Danila, M., Radoi, A., 2014. Mater. Chem. Phys. 146 (3), 538–544.
Chen, N., He, Y., Su, Y., Li, X., Huang, Q., Wang, H., Zhang, X., Tai, R., Fan, C., 2012. Biomaterials 33 (5), 1238–1244.
Chu, X., Duan, D., Shen, G., Yu, R., 2007. Talanta 71 (5), 2040–2047.
Effkemann, S., Pinkernell, U., Karst, U., 1998. Anal. Chim. Acta 363 (1), 97–103.
Fang, Y., Zhang, D., Qin, X., Miao, Z., Takahashi, S., Anzai, J.I., Chen, Q., 2012. Electrochim. Acta 70, 266–271.
Geim, A.K., Novoselov, K.S., 2007. Nat. Mater. 6 (3), 183–191.
Guo, S., Wen, D., Zhai, Y., Dong, S., Wang, E., 2010. ACS Nano 4 (7), 3959–3968.
Han, S., Wu, D., Li, S., Zhang, F., Feng, X., 2014. Adv. Mater. 26 (6), 849–864.
Harman, D., 1981. Proc. Natl. Acad. Sci. USA 78 (11), 7124–7128.
Hummers Jr, W.S., Offeman, R.E., 1958. J. Am. Chem. Soc. 80 (6), 1339.
Ipe, B.I., Lehnig, M., Niemeyer, C.M., 2005. Small 1 (7), 706–709.
Jiang, L., Fan, Z., 2014. Nanoscale 6 (4), 1922–1945.
Jou, A.F.-j., Tai, N.-H., Ho, J.-a.A., 2014. Electroanalysis 26 (8), 1816–1823.
Klassen, N.V., Marchington, D., McGowan, H.C.E., 1994. Anal. Chem. 66 (18), 2921–2925.
Li, M., Bo, X., Zhang, Y., Han, C., Guo, L., 2014. Biosens. Bioelectron. 56, 223–230.
Liu, Q., Yang, Y., Li, H., Zhu, R., Shao, Q., Yang, S., Xu, J., 2014. Biosens. Bioelectron. 64, 147–153.
Liu, Z., Zhao, B., Shi, Y., Guo, C., Yang, H., Li, Z., 2010. Talanta 81 (4–5), 1650–1654.
Lobnik, A., Ajlakovi, M., 2001. Sens. Actuat. B: Chem. 74 (1–3), 194–199.
Maruyama, W., Dostert, P., Matsubara, K., Naoi, M., 1995. Free Radic. Biol. Med. 19 (1), 67–75.
Noh, H.-B., Lee, K.-S., Chandra, P., Won, M.-S., Shim, Y.-B., 2012. Electrochim. Acta 61 (0), 36–43.
Novoselov, K.S., Geim, A.K., Morozov, S.V., Jiang, D., Zhang, Y., Dubonos, S.V., Grigorieva, I.V., Firsov, A.A., 2004. Science 306 (5696), 666–669.
Ohshima, H., Tatemichi, M., Sawa, T., 2003. Arch. Biochem. Biophys. 417 (1), 3–11.
Pagliari, F., Mandoli, C., Forte, G., Magnani, E., Pagliari, S., Nardone, G., Licoccia, S., Minieri, M., Di Nardo, P., Traversa, E., 2012. ACS Nano 6 (5), 3767–3775.
Privett, B.J., Shin, J.H., Schoenfisch, M.H., 2010. Anal. Chem. 82 (12), 4723–4741.
Rhee, S.G., 2006. Science 312 (5782), 1882–1883.
Shoji, E., Freund, M.S., 2001. J. Am. Chem. Soc. 123 (14), 3383–3384.
Sint, K., Wang, B., Král, P., 2008. J. Am. Chem. Soc. 130 (49), 16448–16449.
Sun, Y., He, K., Zhang, Z., Zhou, A., Duan, H., 2015. Biosens. Bioelectron. 68C, 358–364.
Trachootham, D., Alexandre, J., Huang, P., 2009. Nat. Rev. Drug Discov. 8 (7), 579–591.
Veal, E.A., Day, A.M., Morgan, B.A., 2007. Mol. Cell 26 (1), 1–14.
Wang, G., Yang, J., Park, J., Gou, X., Wang, B., Liu, H., Yao, J., 2008. J. Phys. Chem. C 112 (22), 8192–8195.
Wu, P., Cai, Z., Gao, Y., Zhang, H., Cai, C., 2011. Chem. Commun. 47 (40), 11327–11329.
Zhang, L., 2008. Biosens. Bioelectron. 23 (11), 1610–1615.
Zhang, L.S., Wong, G.T.F., 1999. Talanta 48 (5), 1031–1038.
Zhang, W., Chen, J., Swiegers, G.F., Ma, Z.F., Wallace, G.G., 2010. Nanoscale 2 (2), 282–286.
Zhang, Y., Bai, X., Wang, X., Shiu, K.K., Zhu, Y., Jiang, H., 2014a. Anal. Chem. 86 (19), 9459–9465.
Zhang, Y., Bo, X., Nsabimana, A., Luhana, C., Wang, G., Wang, H., Li, M., Guo, L., 2014b. Biosens. Bioelectron. 53 (0), 250–256.
Zhou, Y.G., Chen, J.J., Wang, F.B., Sheng, Z.H., Xia, X.H., 2010. Chem. Commun. 46 (32), 5951–5953.